A&A 650, A16 (2021)
https://doi.org/10.1051/0004-6361/202039297

Astronomy & Astrophysics

Parker Solar Probe: Ushering a new frontier in space exploration

Special Issue

Modeling proton and electron heating in the fast solar wind

L. Adhikari[1], G. P. Zank[1,2], L.-L. Zhao[1], M. Nakanotani[1], and S. Tasnim[1]

[1] Center for Space Plasma and Aeronomic Research (CSPAR), University of Alabama in Huntsville, Huntsville, AL 35899, USA
e-mail: la0004@uah.edu
[2] Department of Space Science, University of Alabama in Huntsville, Huntsville, AL 35899, USA

Received 30 August 2020 / Accepted 1 October 2020

ABSTRACT

Context. The Parker Solar Probe (PSP) measures solar wind protons and electrons near the Sun. To study the thermodynamic properties of electrons and protons, we include electron effects, such as distributed turbulent heating between protons and electrons, Coulomb collisions between protons and electrons, and heat conduction of electrons.
Aims. We develop a general theoretical model of nearly incompressible magnetohydrodynamic (NI MHD) turbulence coupled with a solar wind model that includes electron pressure and heat flux.
Methods. It is important to note that 60% of the turbulence energy is assigned to proton heating and 40% to electron heating. We use an empirical expression for the electron heat flux. We derived a nonlinear dissipation term for the residual energy that includes both the Alfvén effect and the turbulent small-scale dynamo effect. Similarly, we obtained the NI/slab time-scale in an NI MHD phenomenology to use in the derivation of the nonlinear term that incorporates the Alfvén effect.
Results. A detailed comparison between the theoretical model solutions and the fast solar wind measured by PSP and Helios 2 shows that they are consistent. The results show that the nearly incompressible NI/slab turbulence component describes observations of the fast solar wind periods when the solar wind flow is aligned or antialigned with the magnetic field.

Key words. magnetohydrodynamics (MHD) – turbulence – waves

1. Introduction

The shear flow caused by the difference between a fast and slow solar wind speed in the inner heliosphere (Coleman 1968) results in a slower cooling rate of the solar wind temperature than predicted by adiabatic cooling $r^{-4/3}$, where r is the heliocentric distance. Turbulence transport model equations have been used to study solar wind heating, and these include turbulent stream shear and pickup ion sources (Zank et al. 1996, 2017, 2018a; Smith et al. 2001, 2006a,b; Breech et al. 2008, 2009; Adhikari et al. 2014, 2015, 2017, 2020a,b; Wiengarten et al. 2015, 2016; Shiota et al. 2017; Engelbrecht & Strauss 2018). These theories confirm that the radial profile of the solar wind proton temperature is nonadiabatic. Recently, Boldyrev et al. (2020) developed a kinetic theory in which the electron temperature decreases as $r^{-2/5}$, indicating that the electron temperature also presents a nonadiabatic radial profile. However, in Boldyrev's model, the electron temperature is caused by the capture and escape of electrons, so there is no heating of electrons by turbulence, which is thought to be responsible for the nonadiabatic radial profile of the electron and proton temperatures. However, the electron heat flux, Coulomb collisions between electrons and protons, as well as wave-particle interactions between electrons and whistler waves (Tang et al. 2020) may also affect the radial evolution of electron and proton temperatures (Cranmer et al. 2009; Breech et al. 2009; Engelbrecht & Strauss 2018; Chhiber et al. 2019) as well as other thermodynamic properties, such as entropy. Recently, Adhikari et al. (2020b) illustrated the role that turbulence played in the increase of entropy throughout the heliosphere.

In the solar wind plasma, solar wind protons, solar wind electrons, and heavy ions are not in thermal equilibrium. These particles exhibit different temperatures and speeds, which are more obvious in the low-density regions with the least frequent Coulomb collisions (Kohl et al. 1998; Kasper et al. 2008). Understanding the plasma properties among different species will help to clarify the kinetic physical processes of energy deposition into plasma.

The mass density and momentum flux of the solar wind are mainly determined by protons. However, the electrons carry approximately half of the thermal energy of the plasma, so it should not be neglected in a complete study. Effects associated with the incorporation of electrons include splitting the turbulent energy into electron and proton heating, electron heat flux, and Coulomb collisions between electrons and protons. Leamon et al. (1998) pointed out that about 60% of the turbulent energy at 1 au is used for proton heating. Breech et al. (2009) partition turbulence energy for proton and electron heating 60:40, respectively (see also, Cranmer et al. 2009). We include electron effects in a coupled nearly incompressible magnetohydrodynamic (NI MHD) phenomenology–solar wind model.

In previous studies (Zank et al. 2017, 2018b,a; Adhikari et al. 2017, 2020a,c), we considered only proton heating by the dissipation of NI MHD turbulence (Zank et al. 2017). This paper develops a more general theoretical model of solar wind plus NI MHD turbulence that includes electron effects. We use this model to study the electron and proton heating and the evolution of the solar wind proton and electron entropy in the fast solar wind. For this, we use the NI MHD turbulence transport model equations of Zank et al. (2017), which describe the evolution of

majority quasi-2D and NI/slab turbulence throughout the heliosphere. Quasi-2D turbulence corresponds to turbulence that has zero frequency transverse fluctuations whose $\boldsymbol{k}$ vector is primarily in the plane orthogonal to the magnetic field – there is a slowly varying component that is not strictly 2D (see, Hunana & Zank 2010; Zank et al. 2017, 2018b). In the NI MHD description, the quasi-2D turbulence is the dominant incompressible fluctuating component. The NI/slab terminology refers to the nearly incompressible component in the NI MHD description – this component contains Alfvén waves (traditionally called slab turbulence), but it also contains zero frequency 2D modes and therefore it is not strictly slab turbulence. The NI refers to "nearly incompressible". The NI/slab component is a minority component in the NI MHD formulation. This includes the energy in forward and backward propagating modes, cross-helicity, residual energy, fluctuating magnetic and kinetic energy, and corresponding correlation lengths. Here, we modify the nonlinear dissipation term for higher order NI/slab residual energy of Zank et al. (2017) to include Alfvén and turbulent small-scale dynamo effects (Zank et al. 2012). We discuss this in detail below. In this study, we compare the theoretical solutions with the fast solar wind of the first orbit Parker Solar Probe (PSP) and Helios 2.

We organize the manuscript as follows. Section 2 presents the coupled NI MHD turbulence plus solar wind model, including electron effects. In Sect. 3, we discuss the comparison between the theoretical and observed results. Section 4 presents a discussion and conclusions.

2. Gas dynamic and NI MHD turbulence transport equations

The force generated by the pressure gradient of the solar wind electrons and protons drives the solar wind from the surface of the Sun to the outer heliosphere (Parker 1958; Verdini et al. 2010; Chhiber et al. 2019; Adhikari et al. 2020c), although the solar wind speed has been observed to slow down in the outer heliosphere because of the pickup ions (Richardson & Wang 2003; Zank et al. 2018a; Elliott et al. 2019). Adhikari et al. (2020b) pointed out that the turbulent shear source can also lead to a decrease in the solar wind speed, but it is not as significant as pickup ions. Here, we study the evolution of turbulence in the fast solar wind in the inner heliosphere, so we do not include the pickup ion source nor the turbulent shear source for now. We note that driving related to shear may be important to the solar wind and coronal heating problem, but this will be examined elsewhere. The evolution of the solar wind density and the solar wind speed can be described by the 1D steady-state continuity and momentum equations in a spherically symmetric coordinate system as

$$\frac{\mathrm{d}}{\mathrm{d}r}(r^2\rho U) = 0; \tag{1}$$

$$\rho U\frac{\mathrm{d}U}{\mathrm{d}r} = -\frac{\mathrm{d}P_p}{\mathrm{d}r} - \frac{\mathrm{d}P_e}{\mathrm{d}r}, \tag{2}$$

where ρ is the solar wind mass density, U is the solar wind speed, P_p is the thermal proton pressure, and P_e is the thermal electron pressure. Equation (1) gives the (conservation of mass flux) $r^2\rho U = \mathrm{const}$, indicating that the solar wind density decreases as r^{-2} only when the solar wind speed is constant. We assume that the electron density and the proton density are approximately equal, that is to say $n_\mathrm{e} \approx n_\mathrm{p}$. In Eq. (2), we do not include the magnetic force $(\mathbf{J}\times\mathbf{B})_r = -1/(\mu_0 r)B_\phi \mathrm{d}/\mathrm{d}r(rB_\phi)$. We calculate the magnetic force from the Parker spiral (not shown in this manuscript), which is two orders of magnitude smaller than that of protons and electrons. Under the assumption of spherically expansion, the 1D steady-state transport equations for the proton and electron pressure in a spherical coordinate system r can be written in the form,

$$U\frac{\mathrm{d}P_\mathrm{p}}{\mathrm{d}r} + \gamma P_\mathrm{p}\frac{\mathrm{d}U}{\mathrm{d}r} + 2\gamma\frac{U}{r}P_\mathrm{p} = (\gamma-1)\left(\nu_\mathrm{pe}(P_\mathrm{e}-P_\mathrm{p}) + f_\mathrm{p}S_\mathrm{t}\right); \tag{3}$$

$$U\frac{\mathrm{d}P_\mathrm{e}}{\mathrm{d}r} + \gamma P_\mathrm{e}\frac{\mathrm{d}U}{\mathrm{d}r} + 2\gamma\frac{U}{r}P_\mathrm{e} = (\gamma-1)\left[\nu_\mathrm{ep}(P_\mathrm{p}-P_\mathrm{e}) - \nabla\cdot q_\mathrm{e} + (1-f_\mathrm{p})S_\mathrm{t}\right], \tag{4}$$

where S_t is a turbulent heating term, f_p denotes the fraction of the turbulent energy that heats the solar wind protons and $(1-f_\mathrm{p})$ denotes the fraction of turbulent energy that heats the solar wind electrons, $\gamma(=5/3)$ is the polytropic index, and ν_pe and ν_ep are the rates of proton-electron Coulomb collisions (Barakat & Schunk 1982; Zank 2014). The Coulomb collision frequencies are balanced, therefore; $n_\mathrm{e}\nu_\mathrm{ep} \approx n_\mathrm{p}\nu_\mathrm{pe}$. The $P_\mathrm{e}-P_\mathrm{p}$ term in Eqs. (3)–(4) models Coulomb collisions, through which the electrons and protons exchange heat over a timescale $1/\nu_\mathrm{ep} \sim 1/\nu_\mathrm{pe}$. For ν_pe, we use an expression given by Cranmer et al. (2009),

$$\nu_\mathrm{pe} \approx 8.4\times10^{-9}\left(\frac{n_\mathrm{e}}{2.5\ \mathrm{cm}^{-3}}\right)\left(\frac{T_\mathrm{e}}{10^5\ \mathrm{K}}\right)^{-3/2}\ \mathrm{s}^{-1}. \tag{5}$$

Equation (5) is derived by assuming $m_\mathrm{p} \gg m_\mathrm{e}$ and using the rate of temperature equilibrium as described by Spitzer (1962) (see also, Isenberg 1984; Cranmer et al. 1999), and gives a large mean free path of the order of 500−1500 au at 1 au for electron-proton collisions (Cranmer et al. 2009). For electron–electron collisions, the mean free path is found to be of the order of ∼0.5 au at 1 au (see, Spitzer 1962; Salem et al. 2003), which is quite low compared to the mean free path (mfp) of electron-proton collisions. A few authors pointed out that electrons and protons can also exchange energy via collisionless wave-particle interactions (e.g., Cuperman & Harten 1970; Perkins 1973). We note that the collisional term vanishes when $P_\mathrm{e} = P_\mathrm{p}$.

In Eq. (4), the term $\boldsymbol{q}_\mathrm{e}$ is the electron heat flux (the proton heat flux is neglected Braginskii 1965). The effect of the proton heat flux on the proton temperature is less important in comparison to the turbulent heating term. However, the effect of electron heat flux on the electron temperature cannot be excluded. Although we use an isotropic model for the electron and proton temperatures, we use the electron heat flux in the direction parallel to the magnetic field (Cranmer et al. 2009). Because the pressure/temperature contribution is dominated by the Maxwellian core, the parallel and perpendicular contribution to the pressure/temperature are much lower and can be neglected (Tang et al. 2020). Because the core electrons are Maxwellian, their heat flux is zero, and thus heat flux is dominated by the electron strahl. Although, we consider a parallel electron heat flux, we use an empirical formula determined by fitting the observed electron heat flux. In modeling the electron heat flux ($q_\parallel$) along the direction of the magnetic field, the question arises of whether solar wind is collision dominated or collisionless in a particular spatial regime. For a collision dominated model, the Spitzer & Härm (1953) heat flux expression $q_\parallel = -\kappa_\parallel\nabla_\parallel T_\mathrm{e}(r)$ gives a very large temperature at 1 au in contrast to observations (Hollweg 1976). Whereas the collisionless model of Hollweg (1976) produces a reasonable temperature, his model neglects nonlocal effects (Scudder & Olbert 1979). The Hollweg (1976) model

does not consider electron-wave/turbulence scattering, which can affect electron transport significantly (Tang et al. 2020). Cranmer et al. (2009) derived an empirical expression for the electron heat flux $q_\parallel$ by fitting the electron heat flux measured by Helios 2 from 0.3 to 1 au (Pilipp et al. 1990) obtaining,

$$\ln\left(\frac{q_{\parallel,e}}{q_0}\right) = -0.7037 - 2.115x - 0.2545x^2, \tag{6}$$

where $x \equiv \ln(r/1\,\mathrm{au})$ and $q_0 = 0.01$ erg cm^{-2} s^{-1}. Equation (6) is entirely empirical and cannot address whether the solar wind is collisionally dominant or collisionless. The term $\nabla \cdot \boldsymbol{q}_e$ can be expressed in a 1D spherically symmetric coordinate system as (Cranmer et al. 2009)

$$\nabla \cdot \boldsymbol{q}_e = \frac{1}{r^2}\frac{\partial}{\partial r}\left(r^2 q_\parallel \cos^2\phi\right), \tag{7}$$

where ϕ is the Parker spiral angle given by

$$\tan\phi = \frac{\Omega r \sin\theta}{U}, \tag{8}$$

and $\Omega = 2.7 \times 10^{-6}$ rad s^{-1} is the solar rotation frequency. We set a colatitude $\theta = 90°$, because we compare the model results with PSP and Helios 2 measurements in the ecliptic plane.

In addition to Coulomb collisions and the electron heat flux, Eqs. (3)–(4) include a turbulent heating term, in which turbulence energy is distributed between electrons and protons. Here, we assume a constant fraction of $f_p = 0.6$ within 1 au (Leamon et al. 1998), so that 60% of the turbulence energy is used for proton heating, and 40% for electron heating. Breech et al. (2009) used $f_p = 0.6$ throughout the heliosphere, and Howes (2010, 2011), Engelbrecht & Strauss (2018) assumed $f_p = f_p(r)$-however, there is no consensus yet about f_p beyond 1 au.

The turbulent heating term S_t uses a von Kármán phenomenology, and is given by (Verdini et al. 2010; Zank et al. 2018a)

$$\begin{aligned} S_t = \alpha m_p n_s \Bigg[& \frac{\langle z^{\infty+2}\rangle^2\langle z^{\infty-2}\rangle^{1/2}}{L^+_\infty} + \frac{\langle z^{\infty-2}\rangle^2\langle z^{\infty+2}\rangle^{1/2}}{L^-_\infty} \\ & + E^\infty_D\left(\frac{\langle z^{\infty+2}\rangle^{1/2}}{\lambda^-_\infty} + \frac{\langle z^{\infty-2}\rangle^{1/2}}{\lambda^+_\infty}\right) + 2\frac{\langle z^{*+2}\rangle\langle z^{\infty+2}\rangle\langle z^{\infty-2}\rangle^{1/2}}{L^+_\infty} \\ & + 2\frac{\langle z^{*-2}\rangle\langle z^{\infty-2}\rangle\langle z^{\infty+2}\rangle^{1/2}}{L^-_\infty} + \frac{\langle z^{*+2}\rangle^2\langle z^{*-2}\rangle^{1/2}}{L^+_*} \\ & + \frac{\langle z^{*-2}\rangle^2\langle z^{*+2}\rangle^{1/2}}{L^-_*} + E^*_D\left(\frac{\langle z^{\infty-2}\rangle}{\lambda^+_\infty} + \frac{\langle z^{\infty+2}\rangle}{\lambda^-}\right) \\ & - \frac{\langle z^{*+2}\rangle\langle z^{\infty-2}\rangle^{1/2}}{\lambda^+_\infty} - \frac{\langle z^{*-2}\rangle\langle z^{\infty+2}\rangle^{1/2}}{\lambda^-_\infty} \\ & + E^*_D\frac{V_A}{\lambda^+_* + \lambda^-_*}(1-\sigma^*_c)^{1/2}{M^t_{A0}}^2\Bigg], \end{aligned} \tag{9}$$

where "∞" denotes dominant quasi-2D turbulence and "$*$" denotes minority NI/slab turbulence, $\langle z^{+2}\rangle$ denotes the energy in forward propagating modes, $\langle z^{-2}\rangle$ the energy in backward propagating modes, and E_D the residual energy. The parameters L^+ and L^- are the correlation functions corresponding to forward and backward propagating modes and can be expressed by $L^\pm \equiv \langle z^{\pm 2}\rangle\lambda^\pm$, where $\lambda^\pm$ are the correlation lengths of forward and backward propagating modes. The parameter α is the von Kármán-Taylor constant, m_p the proton mass, and n_s the solar wind proton density. The parameter σ^*_c is the normalized cross-helicity, M^t_{A0} is the turbulent Mach number, and we use $M^t_{A0} = 0.1$. This heating term is discussed further below in the context of the dissipation of residual energy. We encourage readers to read Zank et al. (2017), where the detailed derivation of the NI MHD turbulence transport model equations and their definitions are presented.

We do not include the magnetic field in the above equations, but the NI/slab turbulence transport model equations contain the magnetic field in the form of the Alfvén velocity. The magnetic field is assumed to be radial and given by,

$$\mathbf{B} = B_0\left(\frac{r_0}{r}\right)^2\hat{r},$$

where B_0 is the magnetic field at a reference point r_0, and $\hat{r}$ is a unit vector and defines the direction of the magnetic field.

In the NI MHD phenomenology, the turbulence transport equations can be expressed in terms of the majority quasi-2D turbulence and a minority NI/slab turbulence component. Under the assumption of spherical expansion, the 1D steady-state majority quasi-2D turbulence transport model equations are given by (Zank et al. 2017)

$$\begin{aligned} & U\frac{\mathrm{d}\langle z^{\infty\pm2}\rangle}{\mathrm{d}r} + \frac{1}{2}\left(\langle z^{\infty\pm2}\rangle + E^\infty_D\right)\left(\frac{\mathrm{d}U}{\mathrm{d}r} + \frac{2U}{r}\right) \\ & \quad = -2\alpha\frac{\langle z^{\infty\pm2}\rangle^2\langle z^{\infty\mp2}\rangle^{1/2}}{L^\pm_\infty}; \end{aligned} \tag{10}$$

$$\begin{aligned} & U\frac{\mathrm{d}E^\infty_D}{\mathrm{d}r} + \frac{1}{2}(E^\infty_D + E^\infty_T)\left(\frac{\mathrm{d}U}{\mathrm{d}r} + \frac{2U}{r}\right) \\ & \quad = -\alpha E^\infty_D\left(\frac{\langle z^{\infty+2}\rangle^{1/2}}{\lambda^-_\infty} + \frac{\langle z^{\infty-2}\rangle^{1/2}}{\lambda^+_\infty}\right) + \alpha\Bigg(\frac{\langle z^{\infty+2}\rangle\langle z^{\infty-2}\rangle^{1/2}}{\lambda^+_\infty} \\ & \qquad + \frac{\langle z^{\infty-2}\rangle\langle z^{\infty+2}\rangle^{1/2}}{\lambda^-_\infty}\Bigg); \end{aligned} \tag{11}$$

$$U\frac{\mathrm{d}L^\pm_\infty}{\mathrm{d}r} + \frac{1}{2}\left(L^\pm_\infty + \frac{L^\infty_D}{2}\right)\left(\frac{\mathrm{d}U}{\mathrm{d}r} + \frac{2U}{r}\right) = 0; \tag{12}$$

$$U\frac{\mathrm{d}L^\infty_D}{\mathrm{d}r} + \frac{1}{2}\left(\frac{\mathrm{d}U}{\mathrm{d}r} + \frac{2U}{2}\right)(L^\infty_D + L^+_\infty + L^-_\infty) = 0. \tag{13}$$

Here $E^\infty_T = (\langle z^{\infty+2}\rangle + \langle z^{\infty-2}\rangle)/2$ is the quasi-2D total turbulent energy, L^∞_D is the correlation function of the quasi-2D residual energy, and $L^\infty_D \equiv E^\infty_D\lambda^\infty_D$, where λ^∞_D is the correlation length of the quasi-2D residual energy. The parameters $L^\pm_*$ are the correlation functions corresponding to forward and backward propagating modes and $L^\pm_* \equiv \langle z^{*\pm2}\rangle\lambda^\pm_*$, where $\lambda^\pm_*$ are the correlation lengths of NI/slab forward and backward propagating modes). We note that the quasi-2D turbulence couples with the NI/slab turbulence through the second and third terms on the right-hand sides of Eqs. (10) and (11), respectively. The dissipation term for the residual energy in Eq. (11) is different from that of Zank et al. (2017), because the turbulent dynamo effect is included (Grappin et al. 1982, 1983; Zank et al. 2012). Here, the first term on the right hand side (rhs) represents the nonlinear term derived from the Kolmogorov phenomenology (see, Zank et al. 2017), and the second term on the rhs represents the turbulent small-scale dynamo effect (Grappin et al. 1982, 1983; Zank et al. 2012). The turbulent dynamo effect is included in the residual energy because simulations (Grappin et al. 1982, 1983) show that the dynamo effect is present in the MHD turbulence

and controls the evolution of the residual energy. In Eq. (11), the first term on the rhs reduces the residual energy, although the second term on the rhs increases the residual energy. The 1D spherically symmetric transport equations for steady-state NI/slab turbulence are given by (Zank et al. 2017)

$$(U \mp V_{\rm A})\frac{{\rm d}\langle z^{*\pm 2}\rangle}{{\rm d}r} + \frac{1}{2}\frac{{\rm d}U}{{\rm d}r}\left(\langle z^{*\pm 2}\rangle - E_D^*\right) - (2b-1)\frac{U}{r}\langle z^{*\pm 2}\rangle + (6b-1)\frac{U}{r}E_D^* \pm 4b\frac{V_{\rm A}}{r}E_D^* \mp \frac{1}{2}\frac{V_{\rm A}}{\rho}\frac{{\rm d}\rho}{{\rm d}r}\left(\langle z^{*\pm 2}\rangle - E_D^*\right) = -2\alpha\frac{\langle z^{*\pm 2}\rangle\langle z^{\infty\pm 2}\rangle\langle z^{\infty\mp 2}\rangle^{1/2}}{L_\infty^\pm} - 2\alpha\frac{\langle z^{*\pm 2}\rangle^2\langle z^{*\mp 2}\rangle^{1/2}}{L_*^\pm}; \quad (14)$$

$$U\frac{{\rm d}E_D^*}{{\rm d}r} + \frac{1}{2}\frac{{\rm d}U}{{\rm d}r}(E_D^* - E_T^*) - (2b-1)\frac{U}{r}E_D^* + (6b-1)\frac{U}{r}E_T^* - 4b\frac{V_{\rm A}}{r}E_C^* - \frac{1}{2}\frac{V_{\rm A}}{\rho}\frac{{\rm d}\rho}{{\rm d}r}E_C^* = -\alpha E_D^*\left(\frac{\langle z^{\infty -2}\rangle^{1/2}}{\lambda_\infty^+} + \frac{\langle z^{\infty +2}\rangle^{1/2}}{\lambda_\infty^-}\right) + \alpha\left(\frac{\langle z^{*+2}\rangle\langle z^{\infty -2}\rangle^{1/2}}{\lambda_\infty^+} + \frac{\langle z^{*-2}\rangle\langle z^{\infty +2}\rangle^{1/2}}{\lambda_\infty^-}\right) - \alpha E_D^*\frac{V_{\rm A}}{\lambda_*^+ + \lambda_*^-} \times (1-\sigma_c^*)^{1/2}{M_{A0}^t}^2 + \alpha\left(\frac{\langle z^{*+2}\rangle\langle z^{*-2}\rangle^{1/2}}{\lambda_*^+} + \frac{\langle z^{*-2}\rangle\langle z^{*+2}\rangle^{1/2}}{\lambda_*^-}\right); \quad (15)$$

$$(U \mp V_{\rm A})\frac{{\rm d}L_*^\pm}{{\rm d}r} + \frac{1}{2}\left(L_*^\pm - \frac{L_D^*}{2}\right)\frac{{\rm d}U}{{\rm d}r} - (2b-1)\frac{U}{r}L_*^\pm + \left(3b-\frac{1}{2}\right)\frac{U}{r}L_D^* \pm 2b\frac{V_{\rm A}}{r}L_D^* \mp \frac{1}{2}\frac{V_{\rm A}}{\rho}\frac{{\rm d}\rho}{{\rm d}r}\left(L_*^\pm - \frac{L_D^*}{2}\right) = 0; \quad (16)$$

$$U\frac{{\rm d}L_D^*}{{\rm d}r} + \frac{1}{2}(L_D^* - L_*^+ - L_*^-)\frac{{\rm d}U}{{\rm d}r} - \frac{2U}{r}\left[\left(b-\frac{1}{2}\right)L_D^* - \left(3b-\frac{1}{2}\right)\times(L_*^- + L_*^+)\right] - 4b\frac{V_{\rm A}}{r}(L_*^+ - L_*^-) - \frac{1}{2}\frac{V_{\rm A}}{\rho}\frac{{\rm d}\rho}{{\rm d}r}(L_*^+ - L_*^-) = 0, \quad (17)$$

where $V_{\rm A}$ is the Alfvén velocity. The parameter b defines the geometry of NI/slab turbulence. We use $b = 0.33$ (see Zank et al. 2012, 2017, for further discussion). Similarly, we use a von Kármán Taylor constant $\alpha = 0.008$. There is no good physical reason to choose these specific values for b and α, the former of which is related to a closure assumption for off-diagonal 2-point correlations, and the latter to the heating rate associated with nonlinearity. However, we choose these values so that the numerical solutions are close to the observed values. The terms on the right hand sides of Eqs. (10), (11), (14), and (15) are the nonlinear dissipation terms, which are responsible for the decrease in turbulence energy. The nonlinear dissipation terms for the transport equations of the energy in forward and backward propagating modes are derived by assuming a Kolmogorov phenomenology for a fully developed turbulence (see Zank et al. 2012, 2017, 2020). These nonlinear decay terms have been verified by Hossain et al. (1995) through numerical simulations. However, because the residual energy is not a conserved MHD quantity, the modeling of the nonlinear dissipation term for the residual energy is not as obvious as those for the forward and backward propagating modes or for the total turbulent energy. The residual energy is usually negative in the inertial range, that is, the fluctuating magnetic energy is greater than the fluctuating kinetic energy. However, in some cases, the fluctuating kinetic energy can sometimes be greater than the fluctuating magnetic energy, that is, a positive residual energy. To derive the nonlinear term for the residual energy, Zank et al. (2017) followed a Kolmogorov phenomenology (see also, Adhikari et al. 2015). However, Zank et al. (2012) derived another form of the nonlinear term by considering that the Alfvén effect and the turbulent small-scale dynamo effect (Grappin et al. 1982, 1983) control the evolution of the residual energy (see, Zank et al. 2012, for more discussion). Here, we derive a nonlinear term for the residual energy following Zank et al. (2012, 2017, 2020) (see appendix for the derivation), where Zank et al. (2020) introduce the NI/slab time-scale in the NI MHD phenomenology. In Eq. (15), the first term on the rhs is a nonlinear dissipation term derived from a Kolmogorov phenomenology (see, Zank et al. 2017). The second and fourth terms represent the turbulent small-scale dynamo effect in turbulence, which is derived following Zank et al. (2012), that is, we extend dynamo effect to a NI MHD phenomenology. The third term represents the Alfvén effect, which is derived based on Zank et al. (2012), but is slightly modified according to Zank et al. (2020), multiplying by $(1-\sigma_{\rm c}^*)^{1/2}{M_{A0}^t}^2$. When $\sigma_{\rm c}^* = \pm 1$, the third term vanishes, which indicates that the dissipation term related to the Alfvén effect vanishes for the unidirectional Alfvén waves (see, Zank et al. 2020, for a detailed discussion).

NI MHD theory can be used to study the evolution of the variance of the density fluctuations in the solar wind (Zank et al. 2017, 2018a; Adhikari et al. 2017, 2020c). The 1D steady-state transport equation of the density variance is given by (Zank et al. 2017; Adhikari et al. 2017)

$$U\frac{{\rm d}\langle\rho^{\infty 2}\rangle}{{\rm d}r} + 2\langle\rho^{\infty 2}\rangle\frac{{\rm d}U}{{\rm d}r} + 4\frac{U}{r}\langle\rho^{\infty 2}\rangle = -\alpha\frac{\langle u^{\infty 2}\rangle^{1/2}\langle\rho^{\infty 2}\rangle}{l_u^\infty}, \quad (18)$$

where $\langle u^{\infty 2}\rangle = (\langle z^{\infty +2}\rangle + \langle z^{\infty -2}\rangle + 2E_D^\infty)/4$ is the quasi-2D fluctuating kinetic energy and $l_u^\infty = [(E_T^\infty + E_C^\infty)\lambda_\infty^+ + (E_T^\infty - E_C^\infty)\lambda_\infty^- + E_D^\infty\lambda_D^\infty]/2(E_T^\infty + E_D^\infty)$ is the correlation length of the quasi-2D fluctuating kinetic energy. The parameter E_C^∞ is the quasi-2D cross-helicity. In the next section, we present numerical solutions of the solar wind plus NI MHD turbulence transport equations and compare the theoretical results with the PSP and Helios 2 measurements.

3. Results: numerical solutions and observed results

This section presents a comparison between the theoretical results and observations derived from PSP SWEAP (Kasper et al. 2016) and FIELDs (Bale et al. 2016), and Helios 2 measurements. We solve the coupled solar wind and turbulence transport model equations from 45.15 $R_\odot$ to 215 $R_\odot$ using the boundary conditions shown in Table 1, and then we compare the theoretical solutions with the observed results. To compare the model results with PSP observations, we select four intervals in 2018 with start time and end time (DOY:HR:MN): (312:13:0.378–313:8:46.54), (318:1:56.62–319:5:54.51), (319:21:25.64–321:7:59.89), and (323:7:7.16—324.0.46:27.35), where the radial component of the solar wind speed is approximately constant, that is, the plasma is unperturbed (Borovsky 2016). Note that the selected interval corresponds to the fast solar wind flow with average speed of 514.38, 514.29, 559.13, and 464.89 kms^{-1}, respectively, that the PSP first encountered in the outbound direction. The boundary value derived at 45.15 $R_\odot$ is far from the perihelion of the first orbit of PSP (35.55 $R_\odot$) because of the selection of the interval of

Table 1. Boundary values for solar wind parameters and turbulence quantities at 0.21 au (45.15 $R_\odot$).

Parameters	Values	Parameters	Values
$\langle z^{\infty +2}\rangle$	35 008 km^2 s^{-2}	$\langle z^{*+2}\rangle$	17 019.3 km^2 s^{-2}
$\langle z^{\infty -2}\rangle$	3179.6 km^2 s^{-2}	$\langle z^{*-2}\rangle$	907.96 km^2 s^{-2}
E_D^∞	-1134 km^2 s^{-2}	E_D^*	-51.3 km^2 s^{-2}
L_∞^+	1.1×10^{10} km^3 s^{-2}	L_*^+	1.14×10^{9} km^3 s^{-2}
L_∞^-	1.46×10^{9} km^3 s^{-2}	L_*^-	1.53×10^{8} km^3 s^{-2}
L_D^∞	-6.12×10^{9} km^3 s^{-2}	L_D^*	-1.72×10^{8} km^3 s^{-2}
U	530 km s^{-1}	n_p	75.55 cm^{-3}
T_e	3×10^5 K	T_p	5.15×10^5 K
$\langle\rho^{\infty 2}\rangle$	60 cm^{-6}		

Notes. We assume the electron density is approximately equal to the proton density, $n_\mathrm{e}\approx n_\mathrm{p}$. The proton thermal pressure is determined by $P_\mathrm{p}=n_\mathrm{p}k_\mathrm{B}T_\mathrm{p}$ and the electron thermal pressure is determined by $P_\mathrm{e}=n_\mathrm{e}k_\mathrm{B}T_\mathrm{e}$, where k_B is Boltzmann's constant.

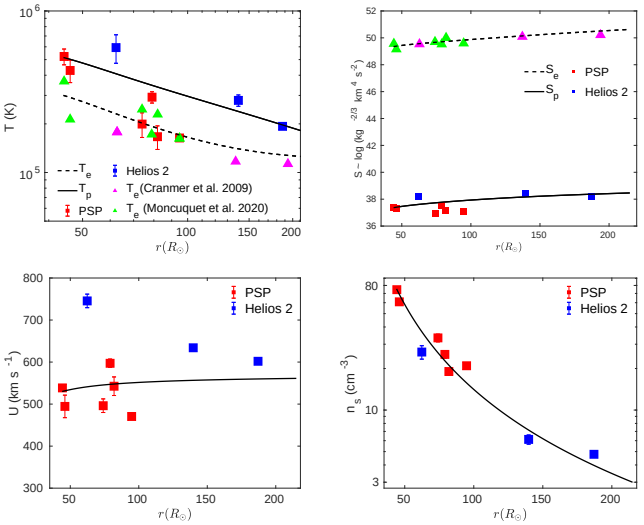

Fig. 1. Comparison between the theoretical (solid and dashed curves) and observed solar wind plasma parameters as a function of heliocentric distance. The red and blue squares are the observed results with error bars. *Top left*: solar wind electron and proton temperature. *Top right*: solar wind proton and electron entropy. *Bottom left*: solar wind speed. *Bottom right*: solar wind density.

unperturbed fast solar wind. The plasma data corresponds to the moment data derived from PSP SWEAP measurements (Kasper et al. 2016). For Helios 2, we select the data intervals at three radial distances 0.29, 0.65, and 0.87 au in 1976, where Helios 2 sampled high-speed streams originating in the same source region at the Sun (Bruno 1992). We derive the turbulent quantities from the measurements of PSP and Helios 2 using a procedure similar to that used in our series of papers (Zank et al. 1996; Adhikari et al. 2014, 2015, 2017; Shiota et al. 2017; Zhao et al. 2018), therefore, we do not describe it here. In deriving the observed values, we employ the criteria that (i) the angle between the large-scale mean flow and the magnetic field should be less than 20° ($\theta_\mathrm{UB}<20°$) and greater than 160° ($\theta_\mathrm{UB}>160°$), and (ii) the mean square fluctuations of the velocity, magnetic field, solar wind density, and solar wind temperature should be lower than the square of their mean fields to avoid data associated with shocks and other embedded structures. Here, we use the NI MHD turbulence transport model equations (Zank et al. 2017) to compare with highly aligned flows measured by PSP and Helios 2 (Telloni et al. 2019; Zhao et al. 2020a). The NI MHD turbulence transport model equations are developed based on the NI MHD phenomenology (Zank & Matthaeus 1992, 1993; Hunana & Zank 2010). In NI MHD theory, quasi-2D turbulence is the dominant component and NI/slab turbulence is a minority component. Previous observations (Telloni et al. 2019; Zhao et al. 2020a) and theory (Zank et al. 2020) have shown that unidirectional Alfvén waves can exhibit a Kolmogorov-like power-law $k^{-5/3}$, where k is the wavenumber, because of the quasi-2D turbulence. Because a spacecraft (PSP) can measure only the NI/slab component in highly aligned flows (Adhikari et al. 2020c), the perpendicular component is essentially invisible.

The dissipation of turbulence heats the solar wind protons and electrons at different rates (Cranmer et al. 2009; Breech et al. 2009; Engelbrecht & Strauss 2018; Chhiber et al. 2019). Similarly, Coulomb collisions between the electrons and protons, and the electron heat flux may influence the solar wind proton temperature and the solar wind electron temperature (Cranmer et al. 2009; Breech et al. 2009; Engelbrecht & Strauss 2018). In this work, we distribute turbulent energy to proton and electron heating in the ratio of 60:40 (Breech et al. 2009), leading to a greater solar wind proton temperature than solar wind electron temperature (see top left panel of Fig. 1). Figure 1 (top left) compares the theoretical and observed solar wind proton and electron temperatures as a function of heliocentric distance. The theoretical solar wind proton temperature (solid curve) decreases as $r^{-0.66}$ with increasing heliocentric distance, which is slower than adiabatic cooling. Similarly, the theoretical solar wind electron temperature (dashed curve) decreases as $r^{-0.54}$ until ~150 $R_\odot$, and then decreases as $r^{-0.24}$ until 215 $R_\odot$. The flattening of the electron temperature between ~150 $R_\odot$ and 215 $R_\odot$ is because of the electron heat flux. Breech et al. (2009) found a shelf-like region in the electron temperature between 1 and 10 au. The red and blue squares denote the solar wind proton temperature measured by PSP and Helios 2, respectively, with error bars, where the error bars denote the interquartile range. Similarly, the green and magenta triangles denote the electron temperature measured by PSP (Moncuquet et al. 2020) and Helios 2 (Cranmer et al. 2009). In PSP measurements, there is no significant difference between the electron and proton temperatures, whereas Helios 2 measurements show a difference of a factor of ~2–6 between them. The results show that the theoretical proton temperature is basically consistent with the observed solar wind proton temperature between 0.2 and 1 au. Similarly, the theoretical solar wind electron temperature is in reasonable agreement with the electron temperature measured by PSP and Helios 2.

The top right plot of Fig. 1 shows the solar wind proton and electron entropy as a function of heliocentric distance. The theoretical and observed solar wind entropy is determined by $S_a\sim\log(P_a/\rho_a^\gamma)$ ($a\equiv(p,e)$, where p denotes a proton and e an electron), where $\gamma=5/3$ is a polytropic index. The solid curve denotes the solar wind proton entropy and the dashed curve the solar wind electron entropy. The red and blue squares describe the observed proton entropy, and the green and magenta triangles the observed electron entropy. The theoretical and observed solar wind proton and electron entropy show that the entropy increases as $r^{0.02}$ with increasing heliocentric distance. Adhikari et al. (2020b) showed that the increase in the solar wind proton entropy is because of the dissipation of turbulence. In addition, Coulomb collisions between electrons and protons, and the heat flux affect entropy. The Coulomb collision term is as a result of the unequal electron and proton temperature ($T_\mathrm{e}\neq T_\mathrm{p}$) (see

the first term on the right-hand side of Eqs. (3) and (4)), which vanishes when $T_e = T_p$. Because the Coulomb collision term becomes negative in Eq. (3) and positive in Eq. (4) because $T_p > T_e$ (see top left panel of Fig. 1), it acts as a source for the electron temperature/pressure/entropy, although it also acts as a sink for the proton temperature/pressure/entropy. Similarly, the electron heat flux term also acts as a source for the electron temperature/pressure/entropy. Therefore, the increase in proton entropy is determined by the dissipation of turbulence, whereas the increase in electron entropy is because of the dissipation of turbulence and the electron heat flux. The effect of Coulomb collisions is negligible compared to the turbulent heating term. If the turbulent heating term is neglected in Eqs. (3) and (4), the proton entropy and electron entropy remain almost constant, the proton temperatures decreases adiabatically, and the solar wind speed decreases very slightly (not shown in this manuscript). However, when the heating term is included, the proton entropy and electron entropy increase modestly by about 2.96 and 2.55% at 1 au from 0.2 au. Figure 1 (top right) shows that the radial profiles of the theoretical proton entropy and electron entropy are consistent with the corresponding observed entropy with increasing heliocentric distance.

In Eqs. (3) and (4), the first term on the left-hand side is the advection term. The second and third terms (a divergence term in a spherical coordinate system r) describe the expansion of the solar wind flow. The right hand side includes turbulent heating, electron heat flux and Coulomb collisions between protons and electrons. For an exclusively adiabatically expanding solar wind, the radial profile of the solar wind proton temperature is $r^{-1.33}$. With the inclusion of the turbulent heating terms, the radial profile of the proton temperature is $r^{-0.65}$, and that of the electron temperature is $r^{-0.54}$ from 45.15 $R_\odot$ to 215 $R_\odot$. However, the electron heat flux also influences the electron temperature.

Figure 1 (bottom left) compares the theoretical and observed solar wind speed as a function of heliocentric distance. As a result of the force generated by the solar wind proton and electron thermal pressure gradients, the theoretical solar wind speed (solid curve) increases slightly with distance. The theoretical solar wind speed is reasonably consistent with the observed solar wind speed (red and blue squares). However, compared with the high-speed flow measured by PSP, Helios 2 measures high speed flow (>700 km s^{-1}) at its perihelion. Similarly, Fig. 1 (bottom right) shows that the theoretical (solid curve) and observed (red and blue squares) solar wind proton density are consistent. The theoretical solar wind density decreases as $r^{-2.03}$.

Figure 2 (top left) compares the theoretical and observed energy in forward propagating modes as a function of heliocentric distance. Here, the solid curve is the theoretical quasi-2D energy in forward propagating modes, which is greater than the observed energy in forward propagating modes. The dashed curve is the minority NI/slab energy in forward propagating modes and its radial profile is similar to that of the observed energy in forward propagating modes. This result is consistent with the results of Adhikari et al. (2020c), in that the theoretical NI/slab turbulent quantities are close to the observed results for fast solar wind during which the velocity and magnetic field are highly aligned or anti-aligned. When modeling the NI MHD turbulence-driven solar wind model for fast solar wind, Adhikari et al. (2020c) explicitly assume that the NI/slab normalized cross-helicity $\sigma_c^* = 1$ and the NI/slab normalized residual energy $\sigma_D^* = 0$, that is, only unidirectional Alfvén waves are present in highly aligned flows, which is consistent with the results of Telloni et al. (2019); Zhao et al. (2020a), and Zank et al. (2020). Telloni et al. (2019) and Zhao et al. (2020a) using

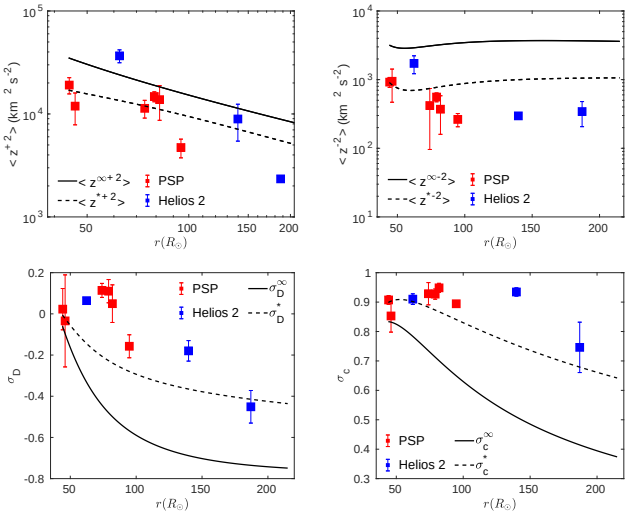

Fig. 2. Comparison between the theoretical and observed turbulent quantities as a function of heliocentric distance. *Top left and right panels*: energy in forward and backward propagating modes. *Bottom left and right*: normalized residual energy and the normalized cross-helicity. The solid curve denotes the quasi-2D component, and the dashed curve represents the slab component. The red and blue squares are the observed quantities measured by PSP and Helios 2 with error bars, respectively.

WIND and PSP measurements of highly aligned flows found that the unidirectional Alfvén waves exhibit a Kolmogorov-like power law spectrum $k^{-5/3}$, where k is the wavenumber. Zank et al. (2020) proposed a detailed NI MHD theory to explain the Kolmogorov power-law spectrum displayed by the unidirectional Alfvén waves. Here, we do not explicitly assume that $\sigma_c^* = 1$ or $\sigma_D^* = 0$, but the observed results are calculated by specifying $\theta_{UB} < 20°$ or $\theta_{UB} > 160°$, where θ_{UB} is the angle between the large-scale solar wind flow and the magnetic field. In this case, PSP and Helios 2 can measure only the minority NI/slab component because quasi-2D fluctuations are effectively invisible to the spacecraft (Telloni et al. 2019; Zhao et al. 2020a; Zank et al. 2020; Adhikari et al. 2020c). The result shows that theoretically and observationally, the energy in forward propagating modes is large near the Sun and decreases with increasing heliocentric distance.

In the top right panel of Fig. 2, there is also reasonable agreement between the observed energy in backward propagating modes and the theoretical NI/slab energy in backward propagating modes, which is again consistent with PSP and Helios 2 being able to measure only the NI/slab NI/slab component in field aligned flows. The energy in backward propagating modes first decreases and then increases slightly with increasing heliocentric distance. Similar to the energy in forward propagating modes, the quasi-2D energy in backward propagating modes is also greater than the observed and NI/slab energy in backward propagating modes. Coleman (1968) suggested that the difference in flow speeds between the fast and slow solar wind produces a turbulent shear source in the inner heliosphere and this turbulent shear source generates the backward propagating modes (Adhikari et al. 2015). However, this turbulent shear source is not included here. In this model, the reflection of forward propagating modes by the solar wind speed, the solar wind density, and the magnetic field gradients produces backward propagating modes.

The normalized residual energy is plotted as a function of heliocentric distance in Fig. 2 (bottom left). The observed

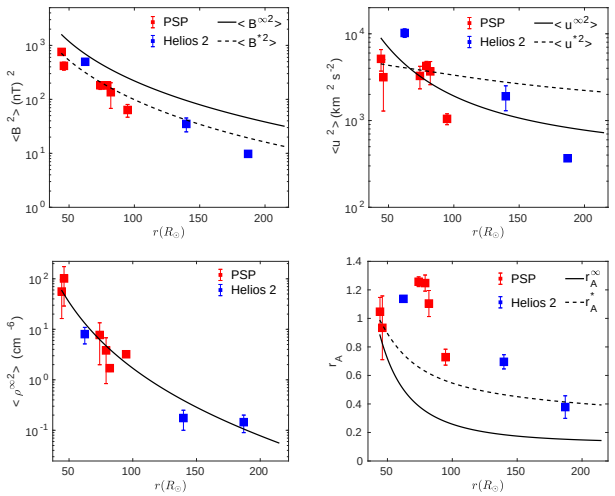

Fig. 3. Comparison between theoretical and observed turbulent quantities as a function of heliocentric distance. *Top left and right panels*: fluctuating magnetic and kinetic energy. *Bottom left and right panels*: variance of the density fluctuations and the Alfvén ratio, respectively. The convention for the curves is the same as used in Fig. 2.

normalized residual energy (red and blue squares) shows that σ_D is close to zero within 100 $R_\odot$, which indicates that the fluctuating kinetic and magnetic energy are approximately equal, that is, Alfvénic, and then decreases with increasing heliocentric distance. This is consistent with the results of Roberts et al. (1987a,b), who found that the Alfvénicity decreases as a function of heliocentric distance. However, this analysis is different from Roberts et al. (1987a,b) because we consider only field aligned flows here. The theoretical NI/slab normalized residual energy (dashed curve) is in reasonable agreement with the observed normalized residual energy, which again indicates that the spacecraft measures a minority NI/slab component when the solar wind flow is aligned or antialigned with the magnetic field (Telloni et al. 2019; Zhao et al. 2020a; Zank et al. 2020; Adhikari et al. 2020c). However, the quasi-2D normalized residual energy (solid curve) decreases more rapidly than the NI/slab normalized residual energy, implying that the quasi-2D turbulence is more magnetically dominated than the NI/slab turbulence. Figure 3 (bottom right) displays the Alfvén ratio $r_A = \langle u^2\rangle/(\langle B^2\rangle/\mu_0\rho)$, that is, the ratio between the fluctuating kinetic and magnetic energy density, as a function of heliocentric distance. The results of the Alfvén ratio and the normalized residual energy are consistent.

The normalized cross-helicity σ_c is a measure of the Alfvénicity of solar wind fluctuations (see, Telloni et al. 2019; Zhao et al. 2020b; Parashar et al. 2020). Figure 2 (bottom right) compares the theoretical and observed normalized cross-helicity as a function of heliocentric distance. In the figure, the observed σ_c (red and blue squares) satisfies $\sigma_c > 0.7$, indicating that the observed solar wind fluctuations are Alfvénic. The observed solar wind fluctuations are more Alfvénic closer to the Sun, where $\sigma_c \sim 0.9$ at heliocentric distance ~45.15 $R_\odot$ in the field aligned flows measured by PSP. The NI/slab normalized cross-helicity (dashed curve) is consistent with the observed σ_c measured by PSP and Helios 2. The quasi-2D normalized cross-helicity near perihelion is assumed to be about 0.83, which decreases rapidly with increasing heliocentric distance. Similar to Fig. 2, this result also clearly shows that the PSP measures minority NI/slab turbulence in the fast wind during which the velocity and magnetic field are closely aligned or anti-aligned. The theoretical and observed normalized cross-helicity decreases with increasing distance, consistent with the results of Roberts et al. (1987a,b). The decrease in the normalized cross-helicity corresponds to the generation of backward modes caused by the reflection of forward propagating modes.

PSP and Helios 2 directly measure the magnetic field. The variance of the magnetic field fluctuations is plotted in Fig. 3 (top left) showing that the theoretical NI/slab fluctuating magnetic energy (dashed curve) is in good agreement with the observed fluctuating magnetic energy (red and blue squares), where the dashed curve decreases as $r^{-2.54}$. The quasi-2D fluctuating magnetic energy (solid curve) is greater than the observed and theoretical NI/slab fluctuating magnetic energy and decreases as $r^{-2.48}$ with increasing heliocentric distance. It is worth noting that the observed fluctuating magnetic variance does not decay as predicted by WKB theory despite the high cross-helicity. The theoretical results of the fluctuating magnetic energy and the energy in forward and backward propagating modes also show that the quasi-2D energy is greater than the NI/slab energy. Only NI/slab components are measured by spacecraft in the highly aligned flows and the theoretical results of the NI/slab components are found to be similar to the observed results. However, in the case of fluctuating kinetic energy, the NI/slab fluctuating kinetic energy may also be greater than the quasi-2D fluctuating kinetic energy (top right panel of Fig. 3) (see also, Zank et al. 2018b). Here, the NI/slab fluctuating kinetic energy is greater than the quasi-2D fluctuating kinetic energy beyond ~66 $R_\odot$. The theoretical quasi-2D fluctuating kinetic energy (solid curve) is in good agreement with the observed fluctuating kinetic energy.

Understanding the variance of the density fluctuations is important for estimating the angular broadening of radio sources in the inner and outer heliosphere, and very local interstellar medium (VLISM) (Bastian 1994; Tasnim et al. 2020). Adhikari et al. (2020c) found that the variance of the density fluctuations in the fast solar wind in the open field region decays as $r^{-6.1}$, and that in the slow solar wind in the outer heliosphere decays as $r^{-2.98}$ (Adhikari et al. 2020a). The variance of the density fluctuations measured by PSP and Helios 2 (red and blue squares) and the theoretical variance of the density fluctuations (solid curve) are plotted in Fig. 3 (bottom left). Both observations and theory are in good agreement, and decrease as $r^{-4.53}$. Although Adhikari et al. (2020c) and this paper study the variance of density fluctuations in the fast solar wind, Adhikari et al. (2020c) study the variance of density fluctuations from the base of the solar corona to 100 $R_\odot$, finding that the variance of density fluctuations drops very rapidly near the base of the solar corona.

The correlation length is important for the evolution of turbulence because it controls the decay rate of turbulence, and thus determines the heating rate. Because the heating rate is inversely proportional to the correlation length, the heating rate is strong when the correlation length is small and weak when the correlation length is large (Verdini et al. 2010; Zank et al. 2012). In Fig. 4, we compare the theoretical and observed correlation length/correlation function with increasing heliocentric distance. The top left and right panels of Fig. 4 are the correlation lengths corresponding to the forward and backward propagating modes. The NI/slab correlation length for forward propagating modes (dashed curve) is consistent with the observed correlation length (red and blue squares). The NI/slab correlation length of backward propagating modes (dashed curve) is in reasonable agreement with the observed correlation length of backward propagating modes. The correlation length of the quasi-2D forward and backward propagating modes (solid curve) increases more gradually as a function of heliocentric distance.

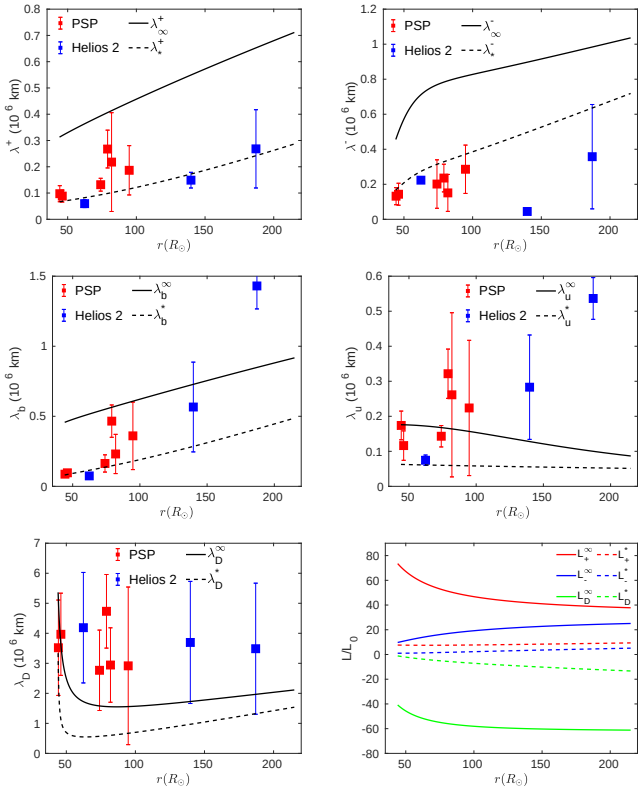

Fig. 4. Correlation length and the correlation function as a function of heliocentric distance. *Top left*: correlation length corresponding to forward propagating modes. *Top right*: correlation length corresponding to backward propagating modes. *Middle left*: correlation length of magnetic field fluctuations. *Middle right*: correlation length of velocity fluctuations. *Bottom left*: correlation length of residual energy. *Bottom right*: correlation functions. The convention for the curve is the same as used in Fig. 2.

The correlation length for the magnetic field fluctuations also increases as distance increases (middle left panel of Fig. 4). The correlation length of the NI/slab fluctuating magnetic energy is in reasonable agreement with the corresponding observed correlation length. However, the correlation length of the quasi-2D fluctuating magnetic energy is greater than the NI/slab correlation length. The observed correlation length for velocity fluctuations also increases with heliocentric distance. However, the quasi-2D fluctuating velocity correlation length decreases with distance, and the correlation length of NI/slab fluctuating kinetic energy is approximately constant (middle left panel of Fig. 4). The results show that the theoretical correlation length for velocity fluctuations is inconsistent with the observed correlation length of velocity fluctuations. This may be as a result of the inclusion of the turbulent dynamo effect. However, with this effect, the theoretical normalized residual energy does not decrease very rapidly. The bottom left panel of Fig. 4 plots the correlation length of the residual energy as a function of heliocentric distance. The theoretical NI/slab and quasi-2D correlation length of residual energy is lower than the observed correlation length, which first decreases and then increases with increasing heliocentric distance. The bottom right panel of Fig. 4 shows the correlation functions corresponding to forward and backward propagating modes, and the residual energy with increasing heliocentric distance. The quasi-2D correlation function corresponding to forward and backward propagating modes (solid red and blue curves) decrease and increase gradually with distance. The quasi-2D correlation function of the residual energy (solid green curve) decreases with distance. Similarly, the NI/slab correlation function corresponding to forward propagating modes (dashed red curve) is approximately constant. The NI/slab correlation function for backward propagating modes (dashed blue curve) increases with distance slightly. Finally, the NI/slab correlation function of the residual energy (dashed green curve) decreases as a function of heliocentric distance.

4. Discussion and conclusions

We developed a very general theoretical model of a nearly incompressible magnetohydrodynamic (NI MHD) turbulence plus solar wind model, including electron pressure and heat flux. In incorporating electrons, we include the splitting of turbulent heating between protons and electrons, Coulomb collisions between protons and electrons, and heat conduction of electrons. The mass density and momentum flux of the solar wind are controlled mainly by solar wind protons, whereas, the thermal energy carried by electrons accounts about similar to that of the protons. Solar wind electrons should not therefore be excluded in a complete treatment of the solar wind. We used a new form of nonlinear dissipation term for the residual energy, different from that of Zank et al. (2017). Zank et al. (2017) derived the nonlinear term for the residual energy following a Kolmogorov phenomenology. However, because the residual energy is not a conserved MHD invariant, modeling of the nonlinear dissipation term for the residual energy is not as obvious as that of the total turbulent energy. Zank et al. (2012) derived the nonlinear dissipation term for the residual energy by following ideas introduced by Grappin et al. (1982, 1983), which includes the Alfvén effect and the turbulent small-scale dynamo effect. We included these effects in the derivation of the nonlinear term for the residual energy, that is, we extended this description to NI MHD phenomenology. In deriving the nonlinear dissipation term for the residual energy related to Alfvén effect, we used the NI/slab time-scale introduced by Zank et al. (2020), which ensures that the nonlinear term vanishes for the unidirectional Alfvén waves, that is, $\sigma_c^* = \pm 1$ (Adhikari et al. 2019).

We compared the theoretical solutions with the fast solar wind measured by PSP and Helios 2. We calculated the observed results by following two criteria: (i) the angle between the large-scale mean flow and the magnetic field should be less than 20° ($\theta_{UB} < 20°$) or greater than 160° ($\theta_{UB} > 160°$), and (ii) the mean square fluctuations of the velocity, magnetic field, solar wind density, and solar wind temperature should be lower than the square their mean fields to avoid data associated with shocks and other embedded structures. Criteria (i) results in PSP and Helios 2 measuring only the NI/slab component, and not quasi-2D component (Telloni et al. 2019; Zhao et al. 2020a). We found good agreement between the theoretical NI/slab results and the observed results. We summarize our main findings as follows.

- The theoretical solar wind proton temperature decreases as $r^{-0.65}$ with increasing distance r and shows reasonable agreement with the observed solar wind proton temperature. The theoretical solar wind electron temperature decreases as $r^{-0.54}$ (where r is heliocentric distance) from 45.15 $R_\odot$ to ~150 $R_\odot$ and then more slowly as $r^{-0.24}$ between ~150 $R_\odot$ and 215 $R_\odot$. The slow decrease in the electron temperature is because of the electron heat flux. The theoretical electron temperature is in reasonable agreement with the observed electron temperature measured by PSP and Helios 2.
- The theoretical and observed solar wind proton entropy and electron entropy are consistent, and increase as $r^{0.02}$

with increasing heliocentric distance. The increase in proton entropy is because of the dissipation of turbulence (Adhikari et al. 2020b), whereas the electron entropy increases as a result of the dissipation of turbulence and the electron heat flux.
- The theoretical NI/slab energy in forward and backward propagating modes, normalized residual energy, normalized cross-helicity, fluctuating magnetic energy, and Alfvén ratio are consistent with the observed values, which indicates that PSP and Helios 2 measure the NI/slab component in the fast solar wind when the large-scale mean flow and the magnetic field are aligned or anti-aligned.
- The observed values of normalized cross-helicity, normalized residual energy, and Alfvén ratio indicate that the fast solar wind is Alfvénic. The Alfvénicity decreases with distance, consistent with observations reported by Roberts et al. (1987a,b). The theoretical NI/slab results are close to the observed values, indicating that the NI/slab turbulence is Alfvénic as well.
- The theoretical and observed variances of the density fluctuations are consistent, and decrease gradually as $r^{-4.53}$.

We used recently developed NI MHD turbulence transport model equations (Zank et al. 2017) to study the evolution of turbulence in the fast solar wind when electron effects are included. It is found that the NI/slab results are close to those observed in the fast solar wind when the flow and the magnetic field are aligned or anti-aligned (see also, Telloni et al. 2019; Zhao et al. 2020a for related observations, and Zank et al. 2020; Adhikari et al. 2020c for related theory). When investigating turbulence evolution in slow solar wind as measured by PSP (Adhikari et al. 2020a), we found that the observed results are close to the quasi-2D component predictions. This in part reflects that the solar wind flow and magnetic field are not necessarily well (anti) aligned in the slow flow. It also likely reflects basic differences in origin of the fast and slow solar wind (e.g., Matthaeus et al. 1990; Bruno & Carbone 2013; Dasso et al. 2005; Wang et al. 2019).

Acknowledgements. We acknowledge the partial support of a Parker Solar Probe contract SV4-84017, an NSF-DOE grant PHY-1707247, and an NSF EPSCoR RII-Track-1 cooperative agreement OIA-1655280. The Parker Solar Probe (PSP) magnetometer and plasma data were obtained from the NASA CDAWeb website.

References

Adhikari, L., Zank, G. P., Hu, Q., & Dosch, A. 2014, ApJ, 793, 52
Adhikari, L., Zank, G. P., Bruno, R., et al. 2015, ApJ, 805, 63
Adhikari, L., Zank, G. P., Hunana, P., et al. 2017, ApJ, 841, 85
Adhikari, L., Zank, G. P., & Zhao, L. L. 2019, ApJ, 876, 26
Adhikari, L., Zank, G. P., Zhao, L. L., et al. 2020a, ApJS, 246, 38
Adhikari, L., Zank, G. P., Zhao, L. L., & Webb, G. M. 2020b, ApJ, 891, 34
Adhikari, L., Zank, G. P., & Zhao, L. L. 2020c, ApJ, 901, 14
Bale, S. D., Goetz, K., Harvey, P. R., et al. 2016, Space Sci. Rev., 204, 49
Barakat, A. R., & Schunk, R. W. 1982, Plasma Phys., 24, 389
Bastian, T. S. 1994, ApJ, 426, 774
Boldyrev, S., Forest, C., & Egedal, J. 2020, ArXiv e-prints [arXiv:2001.05125]
Borovsky, J. E. 2016, J. Geophys. Res. Space Phys., 121, 5055
Braginskii, S. I. 1965, Rev. Plasma Phys., 1, 205
Breech, B., Matthaeus, W. H., Minnie, J., et al. 2008, J. Geophys. Res. Space Phys., 113, 8105
Breech, B., Matthaeus, W. H., Cranmer, S. R., Kasper, J. C., & Oughton, S. 2009, J. Geophys. Res. Space Phys., 114, A09103
Bruno, R. 1992, Solar Wind Seven, COSPAR Colloquia Series, eds. E. Marsch, & R. Schwenn (Oxford; New York: Pergamon Press), 3, 423
Bruno, R., & Carbone, V. 2013, Liv. Rev. Sol. Phys., 10, 2
Chhiber, R., Usmanov, A. V., Matthaeus, W. H., Parashar, T. N., & Goldstein, M. L. 2019, ApJS, 242, 12
Coleman, Jr. P. J. 1968, ApJ, 153, 371
Cranmer, S. R., Field, G. B., & Kohl, J. L. 1999, ApJ, 518, 937
Cranmer, S. R., Matthaeus, W. H., Breech, B. A., & Kasper, J. C. 2009, ApJ, 702, 1604
Cuperman, S., & Harten, A. 1970, ApJ, 162, 315
Dasso, S., Milano, L. J., Matthaeus, W. H., & Smith, C. W. 2005, ApJ, 635, L181
Elliott, H. A., McComas, D. J., Zirnstein, E. J., et al. 2019, ApJ, 885, 156
Engelbrecht, N. E., & Strauss, R. D. T. 2018, ApJ, 856, 159
Grappin, R., Frisch, U., Pouquet, A., & Leorat, J. 1982, A&A, 105, 6
Grappin, R., Leorat, J., & Pouquet, A. 1983, A&A, 126, 51
Hollweg, J. V. 1976, J. Geophys. Res., 81, 1649
Hossain, M., Gray, P. C., Pontius, Jr. D. H., Matthaeus, W. H., & Oughton, S. 1995, Phys. Fluids, 7, 2886
Howes, G. G. 2010, MNRAS, 409, L104
Howes, G. G. 2011, ApJ, 738, 40
Hunana, P., & Zank, G. P. 2010, ApJ, 718, 148
Isenberg, P. A. 1984, J. Geophys. Res., 89, 6613
Kasper, J. C., Lazarus, A. J., & Gary, S. P. 2008, Phys. Rev. Lett., 101, 261103
Kasper, J. C., Abiad, R., Austin, G., et al. 2016, Space Sci. Rev., 204, 131
Kohl, J. L., Noci, G., Antonucci, E., et al. 1998, ApJ, 501, L127
Leamon, R. J., Matthaeus, W. H., Smith, C. W., & Wong, H. K. 1998, ApJ, 507, L181
Matthaeus, W. H., Goldstein, M. L., & Roberts, D. A. 1990, J. Geophys. Res., 95, 20673
Moncuquet, M., Meyer-Vernet, N., Issautier, K., et al. 2020, ApJS, 246, 44
Parashar, T. N., Goldstein, M. L., Maruca, B. A., et al. 2020, ApJS, 246, 58
Parker, E. N. 1958, ApJ, 128, 664
Perkins, F. 1973, ApJ, 179, 637
Pilipp, W. G., Muehlhaeuser, K. H., Miggenrieder, H., Rosenbauer, H., & Schwenn, R. 1990, J. Geophys. Res., 95, 6305
Richardson, J. D., & Wang, C. 2003, AIP Conf. Ser., 679, 71
Roberts, D. A., Goldstein, M. L., Klein, L. W., & Matthaeus, W. H. 1987a, J. Geophys. Res., 92, 12023
Roberts, D. A., Klein, L. W., Goldstein, M. L., & Matthaeus, W. H. 1987b, J. Geophys. Res., 92, 11021
Salem, C., Hubert, D., Lacombe, C., et al. 2003, ApJ, 585, 1147
Scudder, J. D., & Olbert, S. 1979, J. Geophys. Res., 84, 2755
Shiota, D., Zank, G. P., Adhikari, L., et al. 2017, ApJ, 837, 75
Smith, C. W., Matthaeus, W. H., Zank, G. P., et al. 2001, J. Geophys. Res., 106, 8253
Smith, C. W., Isenberg, P. A., Matthaeus, W. H., & Richardson, J. D. 2006a, ApJ, 638, 508
Smith, C. W., Vasquez, B. J., & Hamilton, K. 2006b, J. Geophys. Res. Space Phys., 111, 9111
Spitzer, L. 1962, Physics of Fully Ionized Gases (New York: Dover Publications)
Spitzer, L., & Härm, R. 1953, Phys. Rev., 89, 977
Tang, B., Zank, G. P., & Kolobov, V. I. 2020, ApJ, 892, 95
Tasnim, S., Zank, G. P., Cairns, I. H., & Adhikari, L. 2020, J. Phys. Conf. Ser., 1620, 012022
Telloni, D., Carbone, F., Bruno, R., et al. 2019, ApJ, 887, 160
Verdini, A., Velli, M., Matthaeus, W. H., Oughton, S., & Dmitruk, P. 2010, ApJ, 708, L116
Wang, X., Tu, C., & He, J. 2019, ApJ, 871, 93
Wiengarten, T., Fichtner, H., Kleimann, J., & Kissmann, R. 2015, ApJ, 805, 155
Wiengarten, T., Oughton, S., Engelbrecht, N. E., et al. 2016, ApJ, 833, 17
Zank, G. P. 2014, Transport Processes in Space Physics and Astrophysics, Lect. Notes Phys. (Berlin: Springer Verlag), 877
Zank, G. P., & Matthaeus, W. H. 1992, J. Geophys. Res., 97, 17189
Zank, G. P., & Matthaeus, W. H. 1993, Phys. Fluids, 5, 257
Zank, G. P., Matthaeus, W. H., & Smith, C. W. 1996, J. Geophys. Res., 101, 17093
Zank, G. P., Dosch, A., Hunana, P., et al. 2012, ApJ, 745, 35
Zank, G. P., Adhikari, L., Hunana, P., et al. 2017, ApJ, 835, 147
Zank, G. P., Adhikari, L., Zhao, L. L., et al. 2018a, ApJ, 869, 23
Zank, G. P., Adhikari, L., Hunana, P., et al. 2018b, ApJ, 854, 32
Zank, G. P., Nakanotani, M., Zhao, L. L., Adhikari, L., & Telloni, D. 2020, ApJ, 900, 115
Zhao, L.-L., Adhikari, L., Zank, G. P., Hu, Q., & Feng, X. S. 2018, ApJ, 856, 94
Zhao, L. L., Zank, G. P., Adhikari, L., et al. 2020a, ApJ, 898, 113
Zhao, L. L., Zank, G. P., Adhikari, L., et al. 2020b, ApJS, 246, 26

Appendix A: Nonlinear term for the residual energy

The modeling of the nonlinear dissipation term for the residual energy is not as obvious as that for the total turbulent energy because the residual energy is not a conserved MHD invariant. Zank et al. (2017) derived a nonlinear term for the residual energy by assuming a Kolmogorov phenomenology. We used a similar form of the nonlinear term in our series of papers (Zank et al. 2017, 2018b,a; Adhikari et al. 2017, 2020c,a). Here, we derive a nonlinear term for the residual energy that includes the Alfvén effect and turbulent small-scale dynamo effect. For this, we start with Eq. (22) of Zank et al. (2012),

$$E_D \text{ dissipation term} = -\frac{E_D}{\tau_A^D} + \langle \mathbf{z}^+ \cdot \mathbf{NL}_+ \rangle + \langle \mathbf{z}^- \cdot \mathbf{NL}_- \rangle; \\ = -\frac{E_D}{\tau_A^D} + \frac{\langle z^{+2}\rangle \langle z^{-2}\rangle^{1/2}}{\lambda_+} + \frac{\langle z^{-2}\rangle \langle z^{+2}\rangle^{1/2}}{\lambda_-}, \tag{A.1}$$

where the first term on the rhs defines the Alfvén effect, and the remaining terms define the effect of a turbulent dynamo. The parameter $\tau_A^D \sim \lambda_D/V_\mathrm{A}$ is the relaxation time-scale. We assume $\lambda_D \sim \lambda^+ + \lambda^-$ to avoid a singularity that arises in $\lambda_D \equiv L_D/E_D$ when $E_D = 0$. Equation (A.1) can be written in the form,

$$E_D \text{ dissipation term} \equiv -E_D \frac{V_\mathrm{A}}{\lambda^+ + \lambda^-} + \frac{\langle z^{+2}\rangle \langle z^{-2}\rangle^{1/2}}{\lambda_+} + \frac{\langle z^{-2}\rangle \langle z^{+2}\rangle^{1/2}}{\lambda_-}. \tag{A.2}$$

We derive a nonlinear dissipation term for the residual energy associated with the higher order NI/slab turbulence. We first define the relaxation time for the NI/slab turbulence as

$$\tau_*^D \equiv \frac{\lambda_*^+ + \lambda_*^-}{V_\mathrm{A}} (1 - \sigma_c^*)^{-1/2} {M_{A0}^t}^{-2}, \tag{A.3}$$

where, following Zank et al. (2020), we introduce the $(1 - \sigma_c^*)^{-1/2} {M_{A0}^t}^{-2}$ term, where M_{A0}^t is the turbulent Mach number, and σ_c^* is the normalized cross-helicity. When $\sigma_c^* = \pm 1, \tau_*^D$ is very large, which indicates that there is no energy transfer in the inertial range for unidirectional Alfvén waves (Adhikari et al. 2019). The nonlinear term for the NI/slab residual energy is then given by,

$$E_D^* \text{ dissipation term} = -E_D^* \left(\frac{\langle z^{\infty +2}\rangle}{\lambda_\infty^-} + \frac{\langle z^{\infty -2}\rangle}{\lambda_\infty^+} \right) + \frac{\langle z^{*+2}\rangle \langle z^{\infty -2}\rangle^{1/2}}{\lambda_\infty^+} + \frac{\langle z^{*-2}\rangle \langle z^{\infty +2}\rangle^{1/2}}{\lambda_\infty^-} - E_D^* \frac{V_\mathrm{A}}{\lambda_*^+ + \lambda_*^-} (1 - \sigma_c^*)^{1/2} {M_{A0}^t}^2 + \frac{\langle z^{*+2}\rangle \langle z^{*-2}\rangle^{1/2}}{\lambda_*^+} + \frac{\langle z^{*-2}\rangle \langle z^{*+2}\rangle^{1/2}}{\lambda_*^-}. \tag{A.4}$$

In Eq. (A.4), the first term is similar to that of Zank et al. (2017), which is derived following a Kolmogorov phenomenology. The fourth term defines the Alfvén effect, which is responsible for the decrease in the residual energy, and is zero for unidirectional Alfvén waves. The remaining terms define the turbulence dynamo effect (Grappin et al. 1982, 1983; Zank et al. 2012), which leads to the growth of the residual energy (second, third, fifth and sixth term).

The dissipation term for the quasi-2D residual energy can be written in the form,

$$E_D^\infty \text{ dissipation term} = -E_D^\infty \left(\frac{\langle z^{\infty +2}\rangle}{\lambda_\infty^-} + \frac{\langle z^{\infty -2}\rangle}{\lambda_\infty^+} \right) + \frac{\langle z^{\infty +2}\rangle \langle z^{\infty -2}\rangle^{1/2}}{\lambda_\infty^+} + \frac{\langle z^{\infty -2}\rangle \langle z^{\infty +2}\rangle^{1/2}}{\lambda_\infty^-}, \tag{A.5}$$

where the first term is similar to that of Zank et al. (2017), and the second and third terms represent the turbulent dynamo effect (Grappin et al. 1982, 1983; Zank et al. 2012), which leads to an increase in residual energy.